Information Processing in Agriculture 12 (2025) 358–369

Contents lists available at ScienceDirect

Information Processing in Agriculture

journal homepage: www.keaipublishing.com/en/journals/information-processing-in-agriculture/

A novel method to detect stem and fruit dynamically for apricot posture estimation and adjustment

Wulan Mao [a,b], Leilei He [a], Man Xia [a], Hanhui Jiang [a], Rui Li [a], Ramesh Sahni [d], Yaqoob Majeed [e], Zhanjiang Zhu [b,*], Longsheng Fu [a,c,**]

[a] College of Mechanical and Electronic Engineering, Northwest A&F University, Yangling, Shaanxi 712100, China
[b] Institute of Agricultural Mechanization, Xinjiang Academy of Agricultural Sciences, Urumqi 830000, China
[c] Key Laboratory of Agricultural Internet of Things, Ministry of Agriculture and Rural Affairs, Yangling, Shaanxi 712100, China
[d] Agricultural Mechanization Division, ICAR-Central Institute of Agricultural Engineering, Bhopal 462038, Madhya Pradesh, India
[e] Department of Biological and Agricultural Engineering, Texas A&M University, Dallas, TX 75252, USA

ARTICLE INFO

Keywords:
Apricot
Automated pitting machine
Orientation
Stem
YOLOv8n

ABSTRACT

Separating pulp and core is critical for apricot processing, but faces labor shortages. To address this challenge, a fully automated pitting machine (FAPM) based on automatic apricot orientation device (AAOD) was proposed to achieve mechanized pitting by apricot automatic orientation. The designed and constructed AAOD adopt with dynamic visual detection and mechanical orientation for apricot posture adjustment. YOLOv8 series models were applied for apricot and stem detection, and then estimating their three-dimensional posture. Compared with other YOLOv8 series models, YOLOv8n was selected as the preferred detection model with a detection speed of 10.3 ms and a size of 6.1 MB to meet the need of real-time detection and lightweight deployment. YOLOv8n achieved precision (*P*), recall (*R*), and mean average precision (*mAP*) values of 82.0 %, 90.9 %, and 90.1 %, respectively. Moreover, new indicators, namely positional offsets in the image coordinate system ($Offset_{img}$), positional offsets ($Offset_{3D}$), angular offsets in the 3D coordinate system ($Offset_{ang}$), and the ratio of intersection to manual bounding box areas ($Ratio_{im}$), were proposed to validate the performance of AAOD for position estimation in three varieties of apricot. The best performance was obtained in Saimaiti apricot and achieved $Offset_{img}$ of 2.9 pixels, $Offset_{3D}$ of 1.2 mm, and $Offset_{ang}$ of 0.9°, with $Ratio_{im}$ for apricot and stem were 99.3 % and 97.3 %. Experimental show that the optimal operating parameters for AAOD are 20 rps for alignment wheel rotation speed and the distance of 22.5 mm from apricot base to alignment wheel axis, which presented the best successful orientation rate of 91.5 % with an $Offset_{3D}$ of 1.8 mm. Result demonstrated that the dynamic detection-based orientation approach proposed in this study has great potential for automatic apricot pitting.

1. Introduction

Separation of pulp and core of apricots is a crucial and preliminary step prior to further processing. As a climacteric fruits with a short storage period, apricots require immediate processing after harvest to enhance potential economic value and extend shelf life [1–3]. Consequently, separating apricot pulp and core at the place of origin proves to be an effective approach in addressing the issue of a limited storage period and reducing transportation expenses [4,5]. However, pitting of apricots continues to confront persistent labor shortages [6]. To address this challenge, developing pitting machines is alternative to mitigate labor constraints [7].

The current level of automation in existing pitting machines is relatively low, with tasks such as apricot core removal being automated, while adjustment posture of apricot still heavily relies on manual labor. Precise orientation of apricots is a key step in reducing pulp loss and economic waste during the pitting process. Orientation requires stem position to deviate from the center of punch needle by less than 5 mm to

* Corresponding author at: Institute of Agricultural Mechanization, Xinjiang Academy of Agricultural Sciences, Urumqi 830000, China.
** Corresponding author at: College of Mechanical and Electronic Engineering, Northwest A&F University, Yangling, Shaanxi 712100, China.
E-mail addresses: maowulan@nwafu.edu.cn (W. Mao), hll2023@nwafu.edu.cn (L. He), manxia@nwafu.edu.cn (M. Xia), jianghanhui@nwafu.edu.cn (H. Jiang), ruili1216@nwafu.edu.cn (R. Li), ramesh.sahni@icar.gov.in (R. Sahni), yaqoob.majeed@ag.tamu.edu (Y. Majeed), zhuzhanjiang@xaas.ac.cn (Z. Zhu), fulsh@nwafu.edu.cn (L. Fu).

https://doi.org/10.1016/j.inpa.2024.12.001
Received 26 December 2023; Received in revised form 28 October 2024; Accepted 2 December 2024
Available online 12 December 2024
2214-3173/© 2024 The Author(s). Published by Elsevier B.V. on behalf of China Agricultural University. This is an open access article under the CC BY-NC-ND license (http://creativecommons.org/licenses/by-nc-nd/4.0/).

prevent damage to structural integrity of apricot pulp [8]. This high standard of orientation make automation difficult, which highly relies on labor force. An experienced worker can typically position an apricot within 3 to 4 s, ensuring the alignment with the stem centered and facing upwards on the tray of the pitting machine [9]. While pitting machines reduce labor demand, their reliance on expertise and experience of workers makes them unsuitable for large-scale production scenarios, thereby necessitating the adoption of mechanical orientation devices.

Currently, three primary methods are commonly used for mechanical fruit orientation. The first method capitalizes on the inherent geometric characteristics of fruits for orientation. For instance, Ma et al. [10] achieved apple orientation by rotating it when an alignment wheel contacts the stem or calyx. However, this method is unsuitable for apricots due to their smaller size and shallower stem cavities, which prevent effective orientation. Another method relies on the shape characteristics of uniaxial symmetric fruits, which naturally tend to align in the same direction after rotation on a transmission belt. Ding et al. [11] employed this method in which apricots move in a plane due to the action of the transmission belt and eventually rotate steadily around their axis. The third method utilizes a conveyor belt with a double-cone roller structure to orient the fruits. Flemmer et al. [12] and Li et al. [13] achieved fruit orientation by using a double roller structure to rotate lychee or apple fruits. These two methods are particularly effective for ellipsoidal fruits, with an orientation success rate exceeding 90% when the difference between the longitudinal diameter and the equivalent diameter exceeds 1.3 mm. However, these methods are inadequate for spherical apricot varieties such as Saimaiti, Kizilang, and Qiaolipan to achieve apricot orientation due to their limited orientation accuracy and the complex structure of the machinery, which incurs substantial maintenance costs [9,14].

Continuous advancements of image detection have great potential to determine the position and posture of fruits. Due to its non-contact nature, rapid processing, and high-precision perception of target objects, dynamic detection has been widely applied in the agricultural production domain [15–20]. Detection technology in agricultural production can replace or assist human visual judgment, offering new automated approaches for a wide range of tasks [21–26]. Kaizu et al. [27] employed a convolutional neural network (CNN) to determine the posture of persimmon fruits in images, achieving a detection accuracy of 0.8 mm for the peduncle root position. Wang et al. [28] developed a visual perception system for robotic apple harvesters that utilizes YOLOv5n to identify apple stems and calyxes in real-time, achieving a grasping accuracy of 0.61 cm. Jódar Lázaro et al. [29] used a neural network to classify four olive scenarios with an error rate of less than 4% for olive pitting. These studies confirm that detecting fruit posture provides the possibility of combining dynamic detection with mechanical orientation, to achieve accurate apricot orientation.

The method of posture adjustment based on dynamic detection has been widely applied in the industrial production domain. Zhang et al. [30] developed a lightweight pose measurement algorithm for workpieces that utilizes YOLOv4-Tiny for the detection and adjustment of workpiece pose in real-time, achieving an adjustment accuracy of 0.42 mm. Zhao et al. [31] used a mobile robot machining system for large-scale workpieces that utilizes a global measurement system for the adjustment of workpiece position, effectively eliminating the tool center point error. Tsai et al. [32] employed a production line for adjusting the inclination angle of the workpiece that utilizes a four-axis manipulator and machine vision to pick up the workpiece and then move it to the specified position. These studies confirm that workpiece pipelined posture adjustment enables the possibility of achieving accurate apricot orientation.

In this study, a fully automatic pitting machine (FAPM) was designed for apricot pitting. One of the actuators of FAPM, an automatic apricot orientation device (AAOD), was developed by combining dynamic detection with mechanical orientation. Dynamic detection employs the YOLOv8 series because of its robustness, simplicity, and speed [33,34]. To enhance the generalization of the detection network, datasets were collected from three apricot varieties: Saimaiti, Qiaolipan, and Kezilang. The detection and orientation accuracies of AAOD were assessed using multiple evaluation indices. Ultimately, the FAPM, under optimal operating parameters, maintained high orientation accuracy while reducing orientation time, thereby enhancing the efficiency of apricot processing operations.

2. Materials and methods

2.1. Operation workflow of FAPM

The FAPM is designed to automatic pitting. An operational principle of the FAPM is illustrated in Fig. 1. The FAPM primarily consists of a feed module, a detection module, an orientation module, a pitting module, and a discharge module. The workflow of FAPM for apricot pitting is depicted in Fig. 2. After the tray is filled with apricots, it moves intermittently to the orientation module. Camera of the detection module captures images of the apricots, comparing two adjacent images to confirm the stationary state of the apricot and detect the position of the stem on the horizontal plane of tray. The rotation axis of the first-row stepping motor in the orientation module is aligned in the direction of transportation and defines this direction as transverse rotation. Subsequently, based on position of the stem, the first-row stepping motor within the orientation module drives transverse rotation of the alignment wheel. Through cross slit of the tray, the alignment wheel applies friction to the apricot, facilitating its rotation. Once the detection module detects that the stem is aligned with the projected axis of the alignment wheel on the horizontal plane of the tray, the stepping motor of the orientation module ceases operation. To prevent interference between the alignment wheel and the tray, the alignment wheel repositions itself to be parallel with the tray.

The automatic orientation of apricots is divided into two steps, with the transverse and longitudinal orientations of apricots achieved in two separate intermittent motion cycles. The apricot, moving intermittently with the conveyor belt, reaches the position above the second-row stepping motor, whose direction of rotation is aligned vertically with the first-row stepping motor. This motor longitudinally rotates the apricot with the alignment wheel, based on the stem position detected by the detection module. Upon alignment of the stem of apricot with central axis of the tray on the horizontal plane, the alignment wheel of second row ceases operation and repositions. Following the row-by-row positional adjustment of each apricot, the tray proceeds with conveyance of the apricots. The apricots, advancing intermittently row by row on the conveyor belt, arrive at the pitting module to undergo the core removal operation. The intermittent cam indexer divider converts the prime power into both intermittent and continuous forms. Continuous power actuates the reciprocating motion of pitting tool through the crank connecting rod mechanism, while intermittent power drives the intermittent movement of conveyor belt, ensuring precise synchronization between conveyance and pitting.

2.2. Design of AAOD

The AAOD was developed to serve as both detection and orientation modules for the FAPM, facilitating apricot posture detection and adjustment. The overall success rate of FAPM depends on three primary factors: detection, orientation, and pitting success rates. Detection

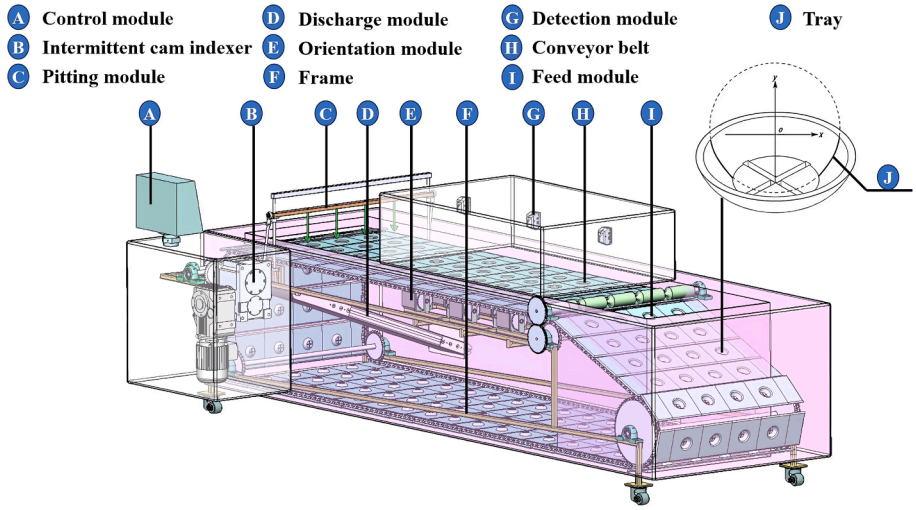


Fig. 1. Diagram of the fully automatic pitting machine (FAPM).

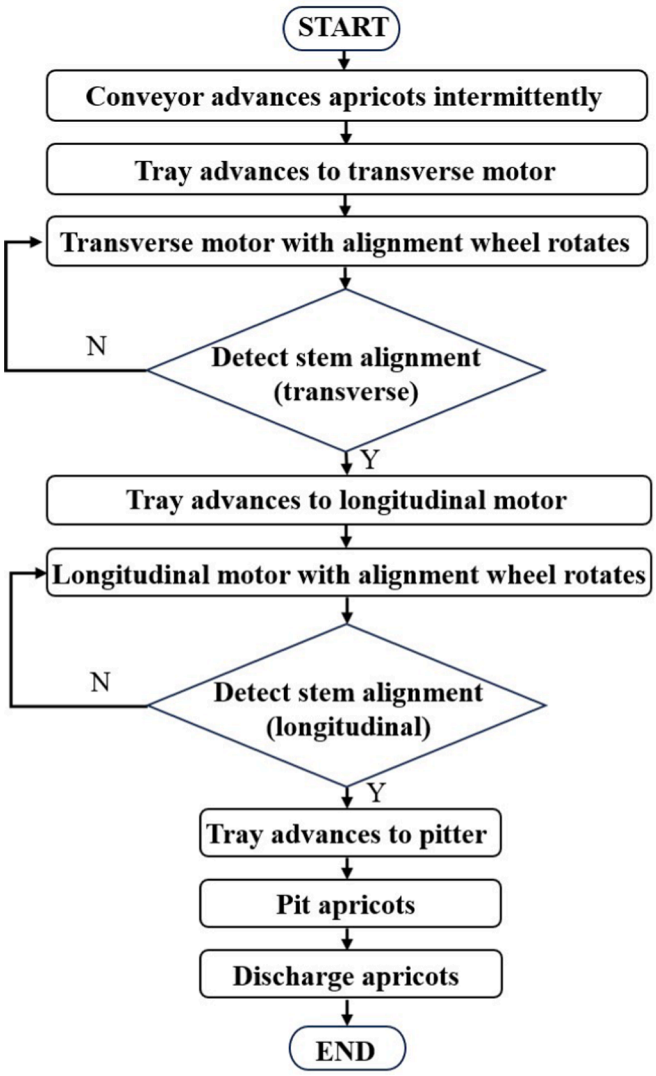


Fig. 2. Workflow of designed FAPM for apricot pitting.

success rate reflects the detection performance of model, accounting for the elimination of false and missed detections. Furthermore, orientation success rate is the proportion of apricots with upward-facing stems among those adjusted. Pitting success rate represents the proportion of apricots with intact pulp relative to total pitting. Therefore, to enhance the overall success rate of FAPM, focus on the AAOD is essential. The structural composition of AAOD, depicted in Fig. 3, includes a camera, tray, alignment stepper motor (ASM), replacement stepper motor (RSM), frame, power source, and an edge computing module.

The camera (2602U, Sudocam Inc., Shenzhen, China) was capable of outputting images at a rate of up to 30 fps. The images were utilized to determine the rotation angle of the ASM. The resolution of camera was set to 1080 × 1080 pixels. The edge computing module outfitted with Nvidia Jetson Nano, operated on an Ubuntu operating system, and the program was developed in Python.

The automatic apricot orientation process commences with the placement of apricots onto the tray, with each apricot assuming an arbitrary posture and the stem oriented in any direction. Upon initiating the Python program, the camera was activated to capture images of the apricots. These images are processed by a pre-trained model to detect the position of the stem. Subsequently, the program signals the ASM, which then rotates to align the stem of apricot transversely (documented time T_1). Once transverse alignment is achieved and the ASM halts, the RSM rotates by 90 degrees (documented time T_2). This rotation permits the longitudinal adjustment of the posture of apricot by the ASM, replication the progression of the tray from the first to the second-row stepping motor in the FAPM and facilitating the change from transverse to longitudinal direction. The program issues a corresponding signal to the ASM to initiate rotation, maneuvering the fruit stem longitudinally until it is aligned with the central position of tray (documented time T_3). If the fruit stem were not within the camera field of vision, the ASM would engage, rotating the apricot until the fruit stem became visible within the camera field of vision. Subsequently, the program would continue to employ the previously described method to adjust posture of the apricot.

Considering actual assembly constraints and average dimensions of apricots, the alignment wheel is designed as a rounded rectangular plate with dimensions of 50 × 10 × 2 mm. The tray is hemispherical with a radius of 25 mm and is crafted from food-grade silicone material, characterized by a Shore hardness of 65. The cross gap of the tray is instrumental in separating the core of apricot and allowing the alignment wheel to make contact with the apricot. If the cross gap is too wide,

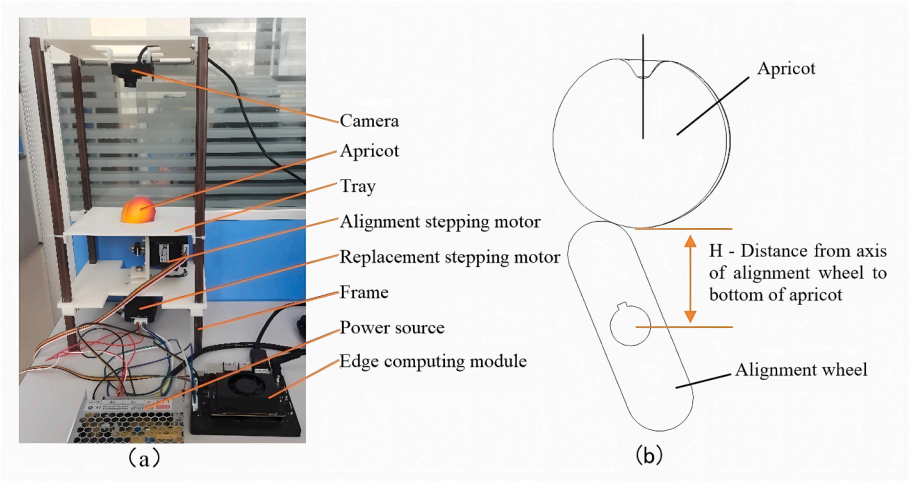


Fig. 3. **(a)** Structural overview of automatic apricot orientation device (AAOD); **(b)** Interaction diagram of alignment wheel and apricot.

apricot flesh is possible to fall through while pitting. On the other hand, a cross gap that is too narrow prevents proper contact between the alignment wheel and the apricot. Hence, the optimal width of the cross gap of tray is set at 3 mm. To minimize interference with the tray and to maximize the contact area with the outer surface of apricot, the width of the alignment wheel is maintained at 2 mm.

When the distance (H) between the axis of the alignment wheel and the bottom of the apricot is 25 mm, the wheel contacts the apricot through the cross gap of tray at the bottom. To produce adequate friction and enable the apricot to rotate, H must be less than 25 mm. If H is less than 21 mm, the force applied by the alignment wheel may eject the apricot from the tray. Consequently, a H ranging from 21 to 25 mm has been determined as optimal. The rotation speed of the alignment wheel (S_{wheel}) also plays a critical role; as it increases, the time to orient the apricot decreases. However, at higher S_{wheel}, the apricot moment of inertia relative to the alignment wheel increases, and at S_{wheel} nearing 40 rps, the apricot may not rotate in unison with the alignment wheel, potentially causing damage to the skin of apricot. Therefore, an S_{wheel} range of 1 to 40 rps has been established. Both the H and S_{wheel} are pivotal factors affecting the accuracy of apricot orientation.

2.3. Apricot sample collection

The experiment investigated the three distinct varieties of apricots: Saimaiti, Qiaolipan, and Kezilang, which exhibit differences in coloration and stem shape, as depicted in Fig. 4. Saimaiti apricots are characterized by a larger average size in comparison to the other two varieties and feature a yellowish hue. In contrast, Kezilang apricots have a reddish coloration, a curvature that closely resembles a sphere, and a stem cavity depth that is shallower than that found in the other varieties. These fruits were cultivated at the Apricot Experimental Station in Yingjisha County, located in the Xinjiang Uygur Autonomous Region of China, with geographical coordinates of 38°57′N, 76°09′E. To minimize the influence of mass variability on the measurement of orientation accuracy, only fruits weighing between 35 and 50 g were selected for the study. On September 5, 2023, a cohort of 100 fresh fruits from each variety, averaging 42.8 ± 7.8 g in weight, were meticulously hand-picked for testing. All apricots were subsequently stored at a temperature of 2°C and 50% relative humidity in preparation.

2.4. Data acquisition and building

At a distance (D_{ot}) of 269 mm from the tray to the origin of camera, the camera field center aligned with center of the tray. During the apricot image collection process, images were captured at a resolution of 1080 × 1080 pixels and subsequently downscaled to 640 × 640 pixels for complying with requirements of YOLOv8 series. Xie & Sun [35] have observed that while downsampling images can reduce computational costs, it tends to compromise detection accuracy due to the reduced resolution. Consequently, to maintain the integrity of the apricot pixels, the original images were cropped to a resolution of 640 × 640 pixels, centered on the tray.

Through the AAOD, 600 images were acquired, comprising three different apricot varieties. Each image was acquired with a single apricot placed in the tray, ensuring that the posture of the apricot was randomized. As depicted in Fig. 5, the apricots in the tray presented the following conditions. In 113 of the 600 placed samples, the stem was facing downwards and was not directly visible. A further 121 samples



Fig. 4. Visual representation of three apricot cultivars. **(a)** Saimaiti; **(b)** Qiaolipan; **(c)** Kezilang.

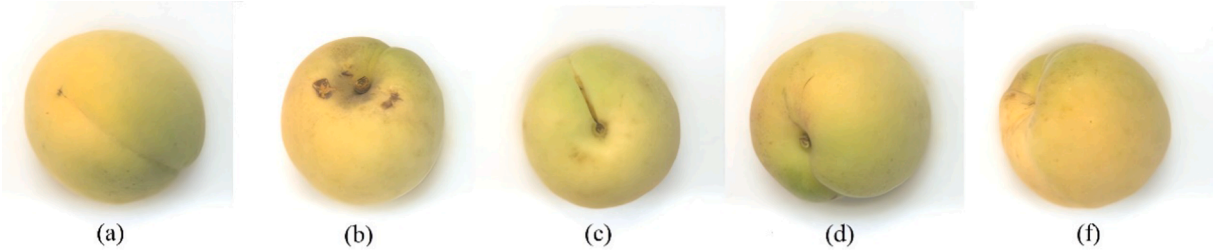


Fig. 5. Five different postures of apricot. (a) Stem facing downwards; (b) Surface damage present; (c) Center of stem facing upwards; (d) Stem directly visible; (e) Stem obscured.

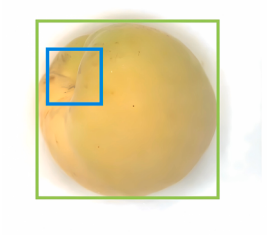


Fig. 6. Bounding boxes of apricot (green rectangle) and stem (blue rectangle).

exhibited surface damage, including breakage. The center of the stem was facing upwards in 50 samples. The stem was directly visible in 180 samples. The position of the stem was obscured by the apricot pulp and was not directly visible in 136 samples. The original images datasets were available on https://github.com/fu3lab/apricot stem fruit-images.

The acquired images were manually annotated using the software tool LabelImg (https://github.com/tzutalin/labelImg), where green and blue rectangular bounding boxes were drawn to label the apricot and stem, respectively, as shown in Fig. 6. For each image, a TXT annotation file was generated that contained object attributes, such as class name, bounding box coordinates, width, and height. Apricots and stems were annotated using rectangular boxes with different class tags in the TXT file. In Fig. 6, the position of the stem is obscured by the pulp of apricot, yet position of the stem could still be discerned. Consequently, when this situation arose, a box with 40 × 40 pixels was drawn around the stem to enable the YOLOv8 series to learn this feature. The bounding boxes were meticulously aligned so that the center of the box coincided with the stem, while also encapsulating the entire outline of stem.

For the experimental procedure, the dataset was divided into three distinct subsets, where 80% allocated for training, 10% for validation, and the remaining 10% designated for testing. Considering apricot postures are largely a function of rotational changes, this study utilized rotational techniques to enrich the training image set, thus yielding a diverse array of apricot postures. Each training image was subjected to both clockwise and counterclockwise rotations about center of the tray, at tenfold intervals of 9 degrees each, as depicted in Fig. 7. The original set of 480 images was expanded to yield a total of 9600 images. This methodology is designed to effectively mitigate overfitting in the trained model while simultaneously enhancing the generalization capabilities of the model.

2.5. Network training

This research retrained prevalent target detection models, encompassing YOLOv8n, YOLOv8s, and YOLOv8m, to ascertain position of the stems. For this experiment, guidance on implementing the YOLOv8 series on Ubuntu using Python was sought from the Ultralytics website (https://github.com/ultralytics/yolov8). To ensure a fair and scientific comparison among the YOLOv8 variants: YOLOv8n, YOLOv8s, and YOLOv8m, this study standardized the computer hardware, parameter configurations, and datasets used for training and testing.

Detection network training was conducted on a desktop computer outfitted with an Intel Core i7-6400 CPU (2.70 GHz), 16 GB of RAM, and an NVIDIA GTX 1080 GPU with 8 GB of memory, operating on a 64-bit Windows 10 environment. The experiments leveraged the Darknet framework, with software tools including CUDA 9.0, cuDNN 7.1.3, and Python 3.6. The input resolution of network was fixed at 640 × 640 pixels, with a batch size of 16. Training was facilitated using stochastic gradient descent, with a momentum parameter set at 0.9 and a weight decay rate of 0.0005. The networks were initialized with a learning rate of 0.01 and an epoch of 300. The mean error and average precision (*AP*) for each learning epoch were documented and assessed. The standard YOLOv8 series configuration file and corresponding weight file were employed for setting the training hyperparameters and initial weights.

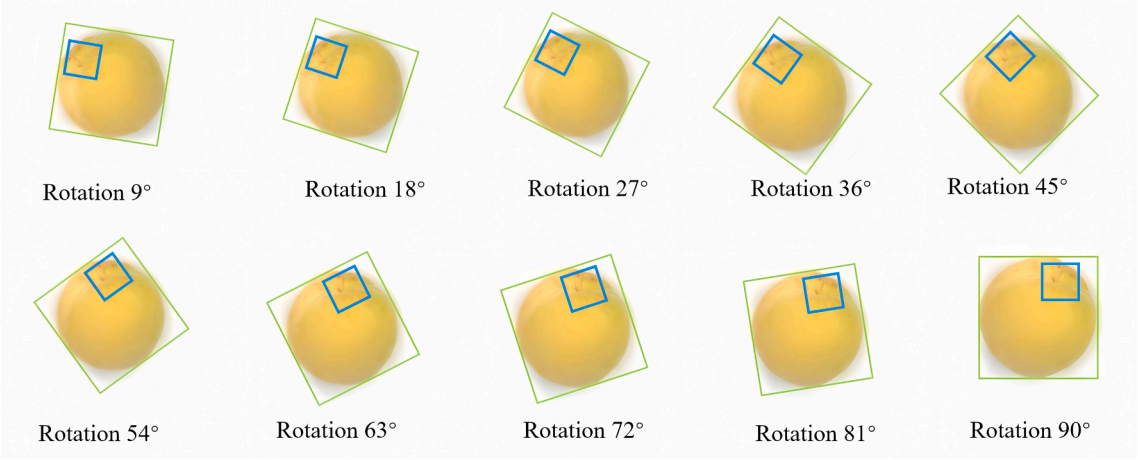


Fig. 7. Examples of image augmentations through center-based rotation.

2.6. Estimation method of stem position

The three-dimension (3D) coordinates of the stem were extrapolated from the predicted bounding box coordinates in the image. The discrepancy between the actual spatial coordinates and the predicted coordinates of the stem was used as a positional offset to assess detection accuracy. The origin of the spatial coordinate system is the camera (O_c), as depicted in Fig. 9. The D_{ot} is the distance between two points P_b and O_c (269 mm), and the projection of the origin (O_c) onto the tray plane coincides with the center of tray (P_b). Two rulers are vertical positioned on the tray plane, and the resulting image is meshed to ascertain the coordinates of the stems, as depicted in Fig. 8. To facilitate subsequent matrix operations, the data are encoded in LabelImg format, with the apricot represented as (0, 0, 0, w_{ai}, h_{ai}) and the fruit stem as (1, x_{si}, y_{si}, w_{si}, h_{si}); the apricot height z_{ai} and fruit stem height z_{si} can be deduced using Eq. (1) and (2).

$$z_{ai} = D_{ot} + R_0 - R_{ai} \tag{1}$$

$$z_{si} = z_{ai} - \sqrt{{R_{ai}}^2 - \left(x_{si}^2 + y_{si}^2\right)} \tag{2}$$

$$R_{ai} = \frac{(w_{ai} + h_{ai})}{4} \tag{3}$$

where R_0 is the radius of the tray within the actual spatial coordinates system (25 mm), which is determined by the average dimensions of apricots; R_{ai} is the average radius of an apricot (mm), which is determined by the width (w_{ai}) and height (h_{ai}) of the manual bounding box of apricot using Eq. (3); D_{ot} is the distance between the camera and the tray (269 mm); In Eq. (1) z_{ai} is the height of the center of the apricot (mm), determined by the distance between two points P_c and O_c; And x_{si}, y_{si}, represent the coordinates of stem center (mm); In Eq. (2) z_{si} is the height of the center of the stem within the actual spatial coordinates system (mm).

The TXT annotation file for the predicted bounding box includes the contents (0, x'_{pai}, y'_{pai}, w'_{pai}, h'_{pai}), and (1, x'_{psi}, y'_{psi}, w'_{psi}, h'_{psi}). In these tuples, 1 is the class identifier for the stem, 0 is the class identifier for the apricot, x and y are the coordinates of the predicted bounding box center, and w and h denote the width and height. Taking the center of the image as the coordinate origin, a reverse normalization operation is conducted. Given that the tray exhibits a hemispherical shape, the center of apricot aligns with the center of tray upon projection onto the plane of tray. Consequently, the coordinates of the apricot are denoted as (0, 0, 0, w_{pai}, h_{pai}), and the coordinates of the stem are represented as (1, x_{psi}, y_{psi}, w_{psi}, h_{psi}), in accordance with Eq. (4) to Eq. (9).

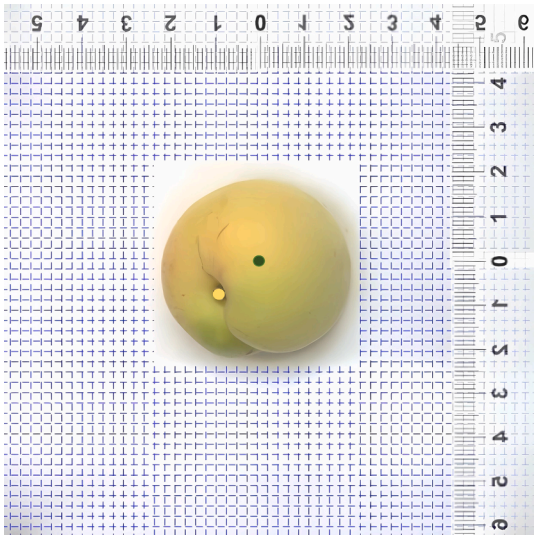


Fig. 8. Actual spatial coordinates of apricot center (green point) and stem center (yellow point).

$$w_{pai} = w'_{pai} \times d \tag{4}$$

$$h_{pai} = h'_{pai} \times d \tag{5}$$

$$w_{psi} = w'_{psi} \times d \tag{6}$$

$$h_{psi} = h'_{psi} \times d \tag{7}$$

$$x_{psi} = x'_{psi} \times d - \frac{d}{2} \tag{8}$$

$$y_{psi} = y'_{psi} \times d - \frac{d}{2} \tag{9}$$

where w_{pai}, and h_{pai}, are the widths and heights of the predicted bounding boxes for apricot, respectively (pixels); In Eqs (6) and (7) w_{psi} and h_{psi} are the widths and heights of the predicted bounding boxes for stem, respectively (pixels); In Eqs (8) and (9) x_{psi}, and y_{psi}, represent the coordinates of stem center (pixels); Each variable with a prime (') denotes the normalized value, which is directly output by the detection model and ranges from 0 to 1; And d is the equivalent dimensions of image width and height, determined by the size of the image input to the model (640 pixels).

$$\lambda = \frac{1}{n}\sum_{i=1}^{n}\frac{w_{pai} + h_{pai}}{w_{ai} + h_{ai}} \tag{10}$$

$$z_{psi} = \lambda z_{ai} - \sqrt{\left(\frac{w_{pai} + h_{pai}}{4}\right)^2 - \left(x_{psi}^2 + y_{psi}^2\right)} \tag{11}$$

where λ is the conversion coefficient that translates the image size (pixels) into real size (mm); And z_{psi} is the height of stem center within the image coordinate system, determined by multiplying z_{si} by λ.

$$offset_{img} = \sqrt{\left(x_{psi} - \lambda x_{si}\right)^2 + \left(y_{psi} - \lambda y_{si}\right)^2} \tag{12}$$

$$offset_{3D} = \sqrt{\left(x_{si} - \frac{x_{psi}}{\lambda}\right)^2 + \left(y_{si} - \frac{y_{psi}}{\lambda}\right)^2 + \left(z_{si} - \frac{z_{psi}}{\lambda}\right)^2} \tag{13}$$

where $Offset_{img}$ is positional offset of stem center within the image coordinate system; And $Offset_{3D}$ is positional offset of stem center within the actual spatial coordinate system, determined by the distance between the predicted coordinates and the real coordinates.

As depicted in Fig. 9, the vector $\vec{F}_c$ denotes the line connecting the stem center (P_p) to the apricot center (P_c), representing the posture of apricot. In the image coordinate system p_p is projection of stem center (P_p), where the predicted and real coordinates are (x_{psi}, y_{psi}) and (x_{si}, y_{si}), respectively. In the image coordinate system p_c is projection of apricot center (P_c), where the predicted and real coordinates are both (0, 0). The predicted and real angle between the vector $\vec{F}_c$ and the z-axis are calculated using Eqs. (14) and (15) based on geometric relations. The angular offset in the actual spatial coordinate system ($Offset_{ang}$) is derived using Eq. (16).

$$\beta_i = arcsin\frac{\sqrt{{x_{si}}^2 + {y_{si}}^2}}{R_{ai}} \tag{14}$$

$$\beta_{pi} = arcsin\frac{\sqrt{{x_{psi}}^2 + {y_{psi}}^2}}{\lambda R_{ai}} \tag{15}$$

$$Offset_{ang} = \left|\beta_i - \beta_{pi}\right| \tag{16}$$

where $Offset_{ang}$ represents the angular offset between the predicted angle

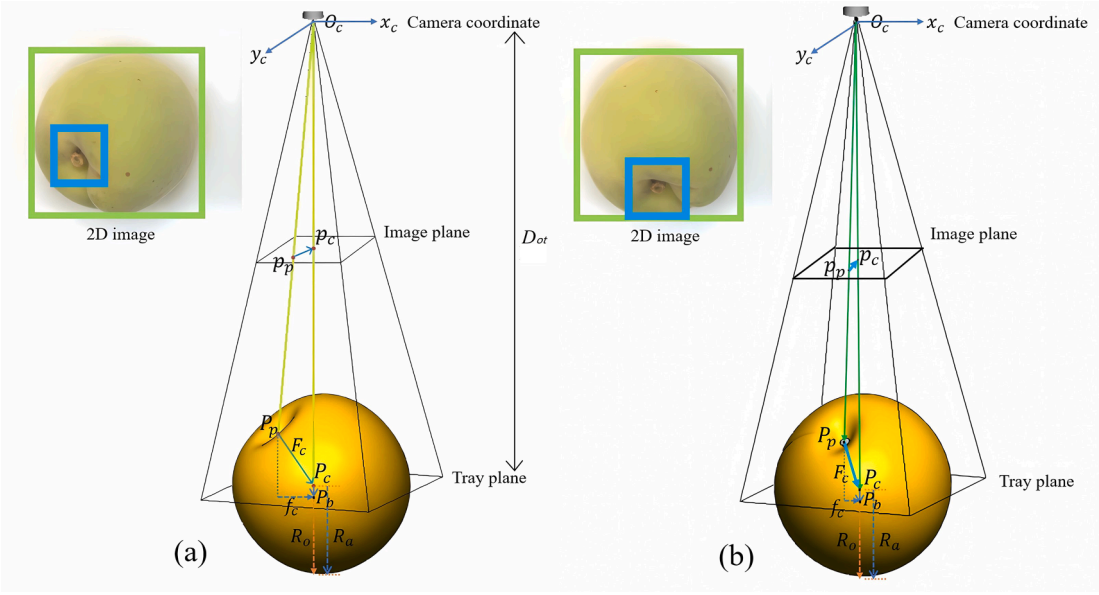


Fig. 9. Estimating 3D coordinates of the stem center. **(a)** Transverse orientation;**(b)** Longitudinal orientation.

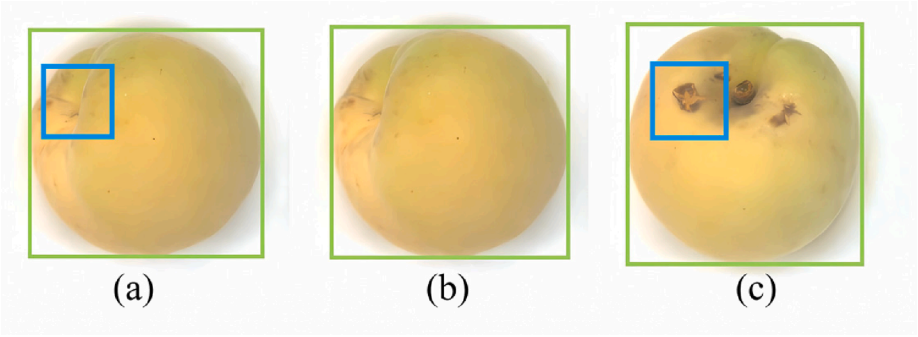


Fig. 10. Illustration of detection outcomes of apricots and stems. **(a)** True positive (*TP*); **(b)** False negative (*FN*); **(c)** False positive (*FP*).

(β_{pi}) and the real angle (β_i); $Offset_{ang}$, $Offset_{img}$, and $Offset_{3D}$ are important evaluation indices of prediction accuracy.

$$f_c = \sqrt{x_{si}{}^2 + y_{si}{}^2} \tag{17}$$

$$Rate_s = \frac{\sum_{i=1}^{n} 1_{\{f_c \le 5\}}}{total_a} \tag{18}$$

where $Rate_s$ is the ratio of successfully oriented apricots to the total number ($total_a$); A projection distance (f_c) of less than 5 mm on the tray plane between two points P_p and P_c in Fig. 9 indicates successful posture adjustment of the apricot, signifying that the stem center is within the target area of the punch needle.

2.7. Evaluation indicators

The performance of apricot and stem detection was assessed using precision (*P*), recall (*R*), *AP*, mean average precision (*mAP*), and average detection speed (S_{det}). Precision (*P*) indicates the proportion of relevant detection results among those retrieved, while *R* is the proportion of truly relevant detection results that were correctly identified. These metrics are defined as per Eq. (19) and Eq. (20), respectively [36]. If an apricot or stem is labeled and detected, as illustrated in Fig. 10**a**, it constitutes a true positive (*TP*). Conversely, if a stem is present but not labeled, as depicted in Fig. 10**b**, it is considered a false negative (*FN*). Furthermore, if a stem is incorrectly detected where none is present, as shown in Fig. 10**c**, it is regarded as a false positive (*FP*).

$$P = \frac{TP}{TP + FP} \tag{19}$$

$$R = \frac{TP}{TP + FN} \tag{20}$$

The integration of *AP* based on accuracy is defined as shown in Eq. (21). The *AP* is defined as the area under P-R curve, which aims to evaluate the performance of model in detecting each class. Meanwhile, the *mAP* is defined as mean *AP* of the two classes (i.e., apricot and stem) in Eq. (22). The value *k* indicates the two classes of objects.

$$AP = \int_0^1 P_{(R)} dR \tag{21}$$

$$mAP = \frac{1}{k}\sum_{i=1}^{k} AP_i \tag{22}$$

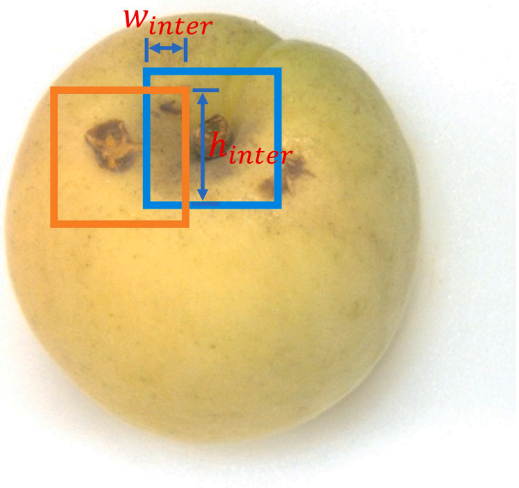


Fig. 11. Comparison between predicted (orange rectangle) and manual labeled (blue rectangle) bounding boxes of detected stem.

The positional precision of apricot and stem detection was evaluated using ratio of intersection to manual bounding box areas ($Ratio_{im}$) and intersection over union (IoU), as detailed in Eq. (25) and (26), respectively. For example, Fig. 11 illustrates the test set with the predicted bounding box indicated in orange and the manual bounding box in blue. The TXT annotation file for the predicted bounding box includes the contents ($1, x_{psi}, y_{psi}, w_{psi}, h_{psi}$), whereas the file for the manual bounding box contains ($1, x_{si}, y_{si}, w_{si}, h_{si}$). In these tuples, 1 is the class identifier for the fruit stem, x and y are the coordinates of the bounding box center, and w and h denote the width and height. The width (w_{inter}) and height (h_{inter}) of the intersection are deducible from Eq. (23) and Eq. (24), respectively. The variability of the data was quantified by the standard deviation (SD), which measures the dispersion of values around the mean, as detailed in Eq. (27).

$$w_{inter} = min\left(\left(x_{psi} + \frac{w_{psi}}{2}\right), \lambda\left(x_{si} + \frac{w_{si}}{2}\right)\right) - max\left(\left(x_{psi} - \frac{w_{psi}}{2}\right), \lambda\left(x_{si} - \frac{w_{si}}{2}\right)\right) \tag{23}$$

$$h_{inter} = min\left(\left(y_{psi} + \frac{h_{psi}}{2}\right), \lambda\left(y_{si} + \frac{h_{si}}{2}\right)\right) - max\left(\left(y_{psi} - \frac{h_{psi}}{2}\right), \lambda\left(y_{si} - \frac{h_{si}}{2}\right)\right) \tag{24}$$

$$IoU = \frac{w_{inter} \times h_{inter}}{w_{psi} \times h_{psi} + w_{si} \times h_{si} \times \lambda^2 - w_{inter} \times h_{inter}} \tag{25}$$

$$Ratio_{im} = \frac{w_{inter} \times h_{inter}}{w_{si} \times h_{si} \times \lambda^2} \tag{26}$$

$$SD = \sqrt{\frac{1}{n}\sum_{i=1}^{n}(f_i - \bar{f})^2} \tag{27}$$

where w_{inter} and h_{inter} are the widths and heights of the intersection areas between the predicted bounding boxes and manual bounding box for stem, respectively (pixels);In Eq. (25) IoU is ratio of the intersection area to the union area between the predicted bounding boxes and the manual bounding box for the stem; In Eq. (26), $Ratio_{im}$ is the ratio of the intersection area to the area of manual bounding box for stem; And λ, f, and SD are the conversion coefficient, variable and standard deviation, respectively.

3. Results and discussion

3.1. Performance comparison of object detection models

The training dataset of apricot images was applied to train YOLOv8n, YOLOv8m, and YOLOv8s. The developed detection models were evaluated using the test dataset. The bounding box loss (*box loss*) values for YOLOv8n, YOLOv8m, and YOLOv8s demonstrated a decrease with an increasing number of epochs, stabilizing around 200 epochs and ultimately converging to their lowest values of 0.28, 0.24, and 0.26, respectively. Fig. 12 presents the evolution of the loss curves over 300 epochs for the training set. Loss curves having converged, which represented that predicted outputs were believable and demonstrated that trained models had learned the apricots and stems for their detection.

Table 1 indicates that the model Sizes for YOLOv8m, YOLOv8s, and YOLOv8n are 50.8 MB, 22.0 MB, and 6.1 MB, respectively. S_{det} were recorded as 25.3 ms for YOLOv8m, 18.6 ms for YOLOv8s, and 10.3 ms for YOLOv8n. This indicates that the S_{det} of YOLOv8m and YOLOv8s were slower than that of YOLOv8n because YOLOv8m and YOLOv8s could be due to more complex network structure increasing inference time. The *mAP* values for the three models exceeded 90%, indicating their high suitability for the detection of apricots and stems. Consequently, YOLOv8n is selected as the preferred detection model due to its superior S_{det} and smaller size, which are advantageous for deployment on an edge computing module. The *mAP* value studied in this paper was higher by 2.1% than the 88% *mAP* achieved by Wang et al. [28], who utilized YOLOv5s for the real-time detection of apple stems and calyxes to facilitate the adjustment of fruit posture.

YOLOv8n achieved *P*, *R*, and *mAP* average values of 82.0%, 90.9%, and 90.1%, respectively. Despite stems are not visible due to the viewing angle, the model can still reliably detect them, as demonstrated in Fig. 13. The model to infer the presence of a stem is attributed not only to the labeled stem but also to the overall characteristics of fruit shape. Result suggests that the ample quantity and diversity of sample images, along with the variety of fruit postures, were sufficient to detect apricot.

3.2. Detection performance of the YOLOv8n for different apricot cultivar

The YOLOv8n was employed to detect three apricot varieties, namely Saimaiti, Qiaolipan, and Kezilang, each distinguished by unique color and shape. Table 2 demonstrates that the YOLOv8n achieved $Ratio_{im}$ scores of 99.3%, 99.1%, and 98.6% for the Saimaiti, Qiaolipan, and Kezilang cultivars, respectively. For the stems of three cultivars, the $Ratio_{im}$ scores were 97.3%, 94.6%, and 90.8%, respectively. The higher $Ratio_{im}$ scores for the apricot cultivars, compared to their stems, can be attributed to the more pronounced color contrast between the apricots and the tray than between the stems and the apricots. Changes in the posture of apricots do not notably alter the shape of fruit, while the appearance of stem varies considerably. Nonetheless, the $Ratio_{im}$ for Kezilang apricot stems was notably lower at 90.8%, compared to the stems of other two cultivars. This difference may be due to the phenotypic characteristics of Kezilang are different from those of other apricots, as depicted in Fig. 14. The phenotypic characteristics of the Kezilang apricot, occupying a minimal proportion of image pixels and potentially obscuring the stem outline, makes detection challenging. Augmenting images of these specific apricot cultivars are a potential solution to address this issue.

YOLOv8n exhibited superior detection capabilities for targets with larger pixel ratios. Table 2 indicates that the YOLOv8n achieved $Offset_{img}$ values of 2.9, 4.9, and 9.5 pixels for the stems of the Saimaiti, Qiaolipan, and Kezilang cultivars, respectively, while the $Offset_{3D}$ values were 1.2 mm, 1.7 mm, and 3.8 mm. It is observed that the Saimaiti cultivar exhibited both $Offset_{img}$ and $Offset_{3D}$ values notably lower than those of the other cultivars. This is likely attributable to the larger average size of the Saimaiti apricots, which results in a higher percentage of stem pixels being fed into the YOLOv8n. Reduction in both $Offset_{img}$ and $Offset_{3D}$

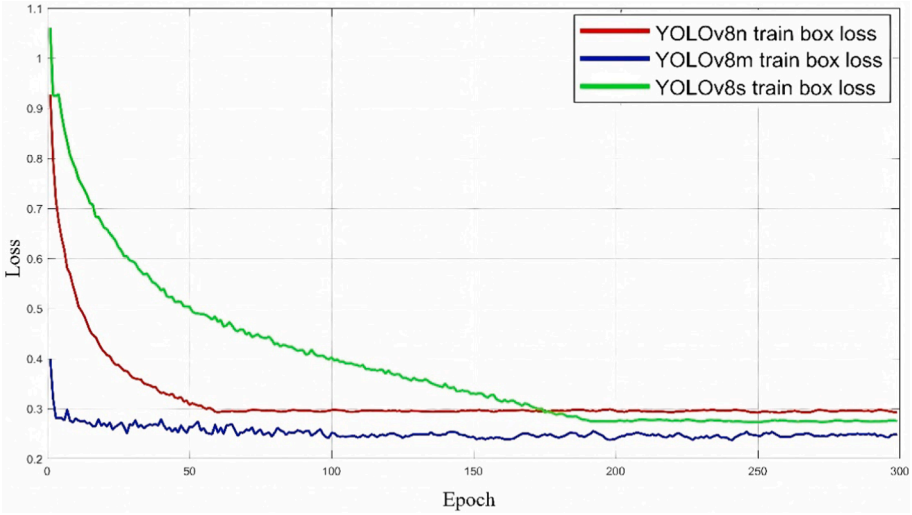


Fig. 12. Loss curves of YOLOv8 series. Red, blue, and green curves represented box-loss curves of YOLOv8n, YOLOv8m, and YOLOv8s, respectively.

Table 1
Detection performance of the three models.

Model	*P* /%	*R* /%	*mAP* /%	S_{det} /ms	*Size* /MB
YOLOv8m	87.4	89.3	93.2	25.3	50.8
YOLOv8s	86.5	91.3	92.2	18.6	22.0
YOLOv8n	82.0	90.9	90.1	10.3	6.1

might be realized by fine-tuning the focal length of the camera lens, which would increase the proportion of pixels of the apricot in the captured images. The $Offset_{3D}$ of the three apricot varieties studied in this paper is higher than the 6.10 mm grasping accuracy achieved by Wang et al. [28], who developed a visual perception system for robotic apple harvesters that utilizes YOLOv5n to identify apple stems and calyxes in real-time.

YOLOv8n demonstrated reduced detection precision at the central positions of targets with smaller pixel ratios. As presented in Table 2, the YOLOv8n achieved *IoU* scores of 98.9%, 98.7%, and 97.5% for the Saimaiti, Qiaolipan, and Kezilang apricot cultivars, respectively, with corresponding stem *IoU* scores of 95.4%, 92.0%, and 88.2%. The *IoU* of apricot was higher than that of the stem due to the larger predicted bounding box surrounding the apricot, which maintained the intersection area of the fruit despite changes in posture. The $Offset_{ang}$ values were 0.9° for the Saimaiti, 1.6° for the Qiaolipan, and 6.1° for the Kezilang. The larger $Offset_{ang}$ for the Kezilang cultivar may be attributed to its smaller size, which reduces the distance between the center of the apricot and position of the stem in the image. Consequently, the $Offset_{3D}$ of the stem notably influences the $Offset_{ang}$ when the radius of the apricot is small.



Fig. 13. Detection of apricot (red rectangle) and stem (orange rectangle) using YOLOv8n in low visibility conditions.

The position of the stem in the image is the most influential factor in adjusting the posture of the apricot. However, a dynamic rather than a static stem was involved while the fruit rotated on the AAOD. Blurring of the stem in the detection images occurred due to the apricot rotation. Prior to the stem reaching the predetermined region, its precise position was not critical provided that the rotation direction of the ASM was ascertained through dynamic detections. This continuous change in posture serves to minimize the impact of the stem $Offset_{img}$ within the image. Consequently, the AAOD developed in this study has potential applications in dynamic stem detection tasks, offering technical support for the dynamic adjustment of apricot posture.

3.3. Optimization of working parameters of AAOD

A response surface diagram was generated by modifying *H* and S_{wheel}, revealing different values of $Offset_{3D}$ after posture adjustment of apricots, as depicted in Fig. 15. The rotation of the apricot, a manifestation of complex nonlinear dynamics, can be notably affected by the alignment wheel, potentially resulting in chaotic behavior within the system.

Table 2
Detection results of the apricot and the stem.

Variety of apricot	Saimaiti		Qiaolipan		Kezilang	
	Apricot	Stem	Apricot	Stem	Apricot	Stem
$Ratio_{im}$ (%)	99.3 ± 0.3[a]	97.3 ± 2.2	99.1 ± 0.4	94.6 ± 5.0	98.6 ± 1.0	90.8 ± 9.8
IoU (%)	98.9 ± 0.5	95.4 ± 2.3	98.7 ± 0.3	92.0 ± 4.9	97.5 ± 0.8	88.2 ± 8.7
$Offset_{img}$[b] (pixels)	2.9 ± 1.7		4.9 ± 3.4		9.5 ± 2.1	
$Offset_{3D}$[c] (mm)	1.2 ± 0.8		1.7 ± 1.5		3.8 ± 4.2	
$Offset_{ang}$[d] (°)	0.9 ± 0.9		1.6 ± 1.7		6.1 ± 7.8	
R_a[e] (mm)	24.8 ± 0.8		24.1 ± 0.8		16.1 ± 0.6	

[a] Mean ± Standard deviation.
[b] $Offset_{img}$ = The positional offset in the image coordinate system.
[c] $Offset_{3D}$ = The positional offset in the 3D coordinate system.
[d] $Offset_{ang}$ = The angular offset in the3D coordinate system.
[e] R_a = The average radius of apricot in the3D coordinate system.

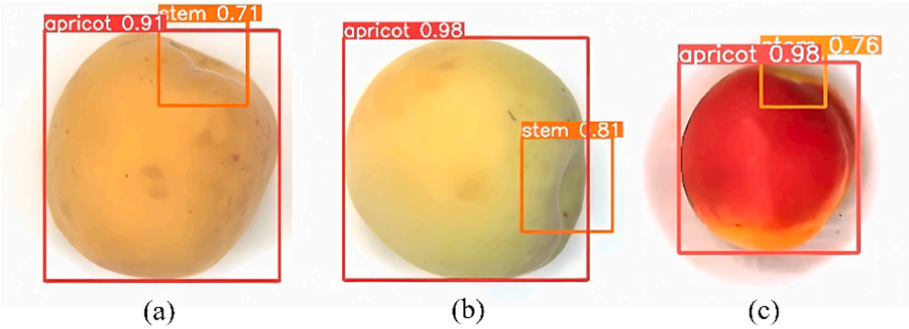


Fig. 14. Detection performance across apricot cultivars in low visibility conditions. **(a)** Saimaiti; **(b)** Qiaolipan; **(c)** Kezilang.

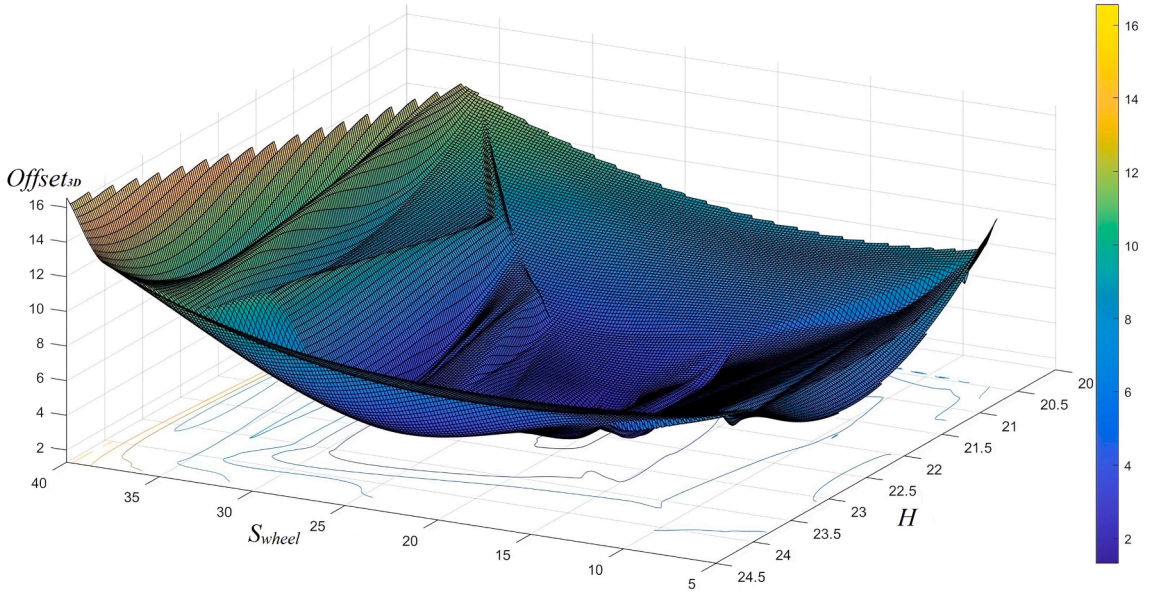


Fig. 15. Response surface diagram of the stem $Offset_{3D}$.

This interaction of the apricot with the alignment wheel introduces additional complexity to the variations in $Offset_{3D}$. A pronounced interactive effect between the S_{wheel} and H affects the $Offset_{3D}$, where an initial gradual decrease is observed, followed by an increase as both variables are increased. The optimal parameter combination for each test variable was determined by identifying the lowest point on the surface, with coordinates (22.5 mm, 20 rps, and 1.8 mm). This suggests that the minimal $Offset_{3D}$, registered at 1.8 mm, is achieved at a S_{wheel} of 20.0 rps and a H of 22.5 mm.

Compared to workpieces in industrial production lines, the individual variability of apricots is significant, resulting in $Offset_{3D}$ for apricots being much lower than the posture adjustment accuracy for workpieces. The $Offset_{3D}$ of 1.8 mm studied in this paper is lower than the 0.42 mm adjustment accuracy achieved by Zhang et al. [30], who developed a lightweight pose measurement model for workpieces that utilizes YOLOv4-Tiny for the detection and adjustment of workpiece pose in real-time. However, an $Offset_{3D}$ of 1.8 mm meets the agronomic requirements for apricot pitting, which require the stem position to deviate from the center of the punch needle by less than 5 mm to prevent damage to the structural integrity of the apricot pulp.

Table 3
Orientation performance of the AAOD.

AAOD	T_1	T_2	T_3
Orientation time (s)	1.5 ± 0.2	0.9 ± 0.1	1.0 ± 0.2

Automatic apricot orientation of AAOD necessitates a total time duration of T, which is the sum of T_1, T_2, and T_3. The ASM requires time T_1 to orient the stem of apricot transversely, followed by the RSM taking time T_2 to rotate by 90 degrees. Subsequently, the ASM requires time T_3 to align the stem of apricot longitudinally. Table 3 indicates that the duration T_1 is greater than T_3 due to continuous rotation of the ASM until the fruit stem is visible within the camera field of vision. Unlike the AAOD, the FAPM operates on an intermittent movement basis, with idle time and movement time. The idle time is closely regulated to approximate T_1 through the use of an intermittent cam indexer and a frequency converter. A single-channel FAPM processes approximately 1200 to 1800 apricots per hour, whereas a four-channel machine can achieve an output of 192 to 360 kg per hour. The AAOD obtained a $Rate_s$ of 91.1%. FAPM utilized the same orientation method and related parameters, satisfying pitting production.

4. Conclusions

This work presents a novel method for adjusting the posture of apricots using the AAOD by combining dynamic detection with mechanical orientation. YOLOv8n is a suitable detection model for inferring the posture of apricots through the geometric relationship between the position of the stem and the diameter of the apricot detected in the image. The stem outline and shape features are beneficial for accurately detecting the position of the stem, especially for the Saimaiti cultivar. Moreover, S_{wheel} of 20 rps and H of 22.5 mm prove that AAOD efficiently

adjusts the posture of apricots and meets agronomic requirements for apricot pitting. In the future, a control program for automatic parameter adjustment is planned, which will update the feature weights of the apricot stem and improve orientation accuracy. The results not only contribute to the field of automated fruit pitting but also have potential applications in the automated processing of other spherical agricultural products with enhanced speed and accuracy.

CRediT authorship contribution statement

Wulan Mao: Writing – original draft, Data curation. **Leilei He:** Methodology, Investigation, Data curation. **Man Xia:** Data curation, Formal analysis, Validation. **Hanhui Jiang:** Software, Conceptualization. **Rui Li:** Writing – review & editing. **Ramesh Sahni:** Investigation. **Yaqoob Majeed:** Supervision, Methodology. **Zhanjiang Zhu:** Validation. **Longsheng Fu:** Writing – review & editing, Resources, Project administration.

Declaration of competing interest

The authors declare that they have no known competing financial interests or personal relationships that could have appeared to influence the work reported in this paper.

Acknowledgements

This work was supported by the Tianshan Top Youth Science and Technology Talent of Xinjiang, China (2022TSYCCX0066); Xinjiang Minority Scientific and Technological Talents Special Training Project (2022D03007); National Natural Science Foundation of China (32171897); and National Foreign Expert Project, Ministry of Science and Technology, China (DL2022172003L, QN2022172006L).

References

[1] Ali Sultan Q, Wahab S. Essential oils affect the development of apricot brown rot during post-harvest storage. Hortic Environ Biotechnol 2023;64(4):643–54. https://doi.org/10.1007/s13580-022-00504-9.
[2] Hua X, Li T, Wu C, Zhou D, Fan G, Li X, et al. Pulsed light improved the shelf life of apricot (after simulated long-distance air transportation) by regulating cell wall metabolism. Postharvest Biol Technol 2023;196:112187. https://doi.org/10.1016/j.postharvbio.2022.112187.
[3] Huang W, Feng Z, Aila R, Hou Y, Carne A, Bekhit AEDA. Effect of pulsed electric fields (PEF) on physico-chemical properties, β-carotene and antioxidant activity of air-dried apricots. Food Chem 2019;291:253–62. https://doi.org/10.1016/j.foodchem.2019.04.021.
[4] Xin Q, Zhou X, Jiang W, Zhang M, Sun J, Cui K, et al. Effects of reactive oxygen levels on chilling injury and storability in 21 apricot varieties from different production areas in China. Foods 2023;12:2378. https://doi.org/10.3390/foods12122378.
[5] Su C, Li T, Wang Y, Ge Z, Xiao J, Shi X, et al. Comparison of phenolic composition, vitamin C, antioxidant activity, and aromatic components in apricots from Xinjiang. J Food Sci 2022;87(1):231–50. https://doi.org/10.1111/1750-3841.16002.
[6] Sanjeevi P, Siva Kumar B, Prasanna S, Maruthupandi J, Manikandan R, Baseera A. An ontology enabled internet of things framework in intelligent agriculture for preventing post-harvest losses. Complex Intell Syst 2021;7(4):1767–83. https://doi.org/10.1007/s40747-020-00183-y.
[7] Salazar JA, Martínez-Gómez P, Ruiz D. Varietal evaluation of postharvest behavior in apricot fruits. Eur J Hortic Sci. 2022;87(1):1–14. https://doi.org/10.17660/eJHS.2022/010.
[8] Mao W, Zhu Z, Yang L, Cui K, Zhu Z. Optimization research and experimental analysis of apricot fruit cutting and de-core mechanism. Xinjiang Agric Sci 2022;59(12):3084–92. https://doi.org/10.6048/j.issn.1001-4330.2022.09.025.
[9] Mao W, Guo J, Zhu Z. Design and experiment of continuous apricot kernel removal machine. Xinjiang Agric Sci 2022;59(9):2295–302. https://doi.org/10.6048/j.issn.1001-4330.2022.09.025.
[10] Ma Y, Yu J. Modeling and dynamic simulation of automatic apple oriented mechanism. Food Mach 2016;32(11):55–8. https://doi.org/10.13652/j.issn.1003-5788.2016.11.012.
[11] Ding XY, Wang CY, Huang CY, Luo JQ. Attitude control of apricot during orientation transmission. Int J Agric Biol Eng 2016;9(5):9–16. https://doi.org/10.3965/j.ijabe.20160905.2135.
[12] Flemmer C, Bakker H, Flemmer R. Analysis of the stochastic excursions of tumbling apples. Comput Electron Agric 2021;188:106362. https://doi.org/10.1016/j.compag.2021.106362.
[13] Li C, Ma X, Cheng H, Chen Z. Design and experiment of litchi denucleating and decorticating machine. Trans Chinese Soc Agric Mach 2014;45(8):93–100. https://doi.org/10.6041/j.issn.1000-1298.2014.08.015.
[14] Yu Y, An X, Lin J, Li S, Chen Y. A vision system based on CNN-LSTM for robotic citrus sorting. Inf Process Agric 2022;11(1):14–25. https://doi.org/10.1016/j.inpa.2022.06.002.
[15] Xiao B, Nguyen M, Yan WQ. Fruit ripeness identification using YOLOv8 model. Multimed Tools Appl 2023;83(9):28039–56. https://doi.org/10.1007/s11042-023-16570-9.
[16] Yang G, Wang J, Nie Z, Yang H, Yu S. A lightweight YOLOv8 tomato detection algorithm combining feature enhancement and attention. Agronomy 2023;13:1824. https://doi.org/10.3390/agronomy13071824.
[17] Xiang Y, Yao J, Yang Y, Yao K, Wu C, Yue X, et al. Real-time detection algorithm for kiwifruit canker based on a lightweight and efficient generative adversarial network. Plants 2023;12:3053. https://doi.org/10.3390/plants12173053.
[18] Assunção E, Gaspar PD, Alibabaei K, Simões MP, Proença H, Soares VNGJ, et al. Real-time image detection for edge devices: a peach Fruit detection application. Futur Internet 2022;14(11):1–12. https://doi.org/10.3390/fi14110323.
[19] Liu B, Zhang Y, Wang J, Luo L, Lu Q, Wei H, et al. An improved lightweight network based on deep learning for grape recognition in unstructured environments. Inf Process Agric 2024;11(2):202–16. https://doi.org/10.1016/j.inpa.2023.02.003.
[20] Ismail N, Malik OA. Real-time visual inspection system for grading fruits using computer vision and deep learning techniques. Inf Process Agric 2022;9(1):24–37. https://doi.org/10.1016/j.inpa.2021.01.005.
[21] Feng J, Wang Z, Wang S, Tian S, Xu H. MSDD-YOLOX: An enhanced YOLOX for real-time surface defect detection of oranges by type. Eur J Agron 2023;149:126918. https://doi.org/10.1016/j.eja.2023.126918.
[22] Li P, Zheng J, Li P, Long H, Li M, Gao L. Tomato maturity detection and counting model based on MHSA-YOLOv8. Sensors 2023;23:6701. https://doi.org/10.3390/s23156701.
[23] Hao Y, Wang Q, Zhang S. Online accurate detection of soluble solids content in navel orange assisted by automatic orientation correction device. Infrared Phys Technol 2021;118:103871. https://doi.org/10.1016/j.infrared.2021.103871.
[24] Zhang M, Liang H, Wang Z, Wang L, Huang C, Luo X. Damaged apple detection with a hybrid YOLOv3 algorithm. Inf Process Agric 2024;11(2):163–71. https://doi.org/10.1016/j.inpa.2022.12.001.
[25] Mao W, Murengami B, Jiang H, Li R, He L, Fu L. UAV-based high-throughput phenotyping to segment individual apple tree row based on geometrical features of poles and colored point cloud. J ASABE 2024;67(5):1231–40. https://doi.org/10.13031/ja.15895.
[26] Yang R, Wu Z, Fang W, Zhang H, Wang W, Fu L, et al. Detection of abnormal hydroponic lettuce leaves based on image processing and machine learning. Inf Process Agric 2023;10(1):1–10. https://doi.org/10.1016/j.inpa.2021.11.001.
[27] Kaizu Y, Miyanishi Y, Todoriki Y, Furuhashi K, Imou K. Detection of persimmon posture by a convolutional neural network for fully automating the peeling process. J ASABE 2022;65(6):1375–86. https://doi.org/10.13031/ja.14452.
[28] Wang Z, Jin L, Wang S, Xu H. Apple stem/calyx real-time recognition using YOLO-v5 algorithm for fruit automatic loading system. Postharvest Biol Technol 2022;185:111808. https://doi.org/10.1016/j.postharvbio.2021.111808.
[29] Jódar Lázaro M, Luna AM, Lucas Pascual A, Martínez JMM, Canales AR, Madueño Luna JM, et al. Deep learning in olive pitting machines by computer vision. Comput Electron Agric 2020;171:105304. https://doi.org/10.1016/j.compag.2020.105304.
[30] Zhang T, Zheng J, Zou Y. Fusing few-shot learning and lightweight deep network method for detecting workpiece pose based on monocular vision systems. Meas J Int Meas Confed 2023;218:113118. https://doi.org/10.1016/j.measurement.2023.113118.
[31] Zhao X, Tao B, Han S, Ding H. Accuracy analysis in mobile robot machining of large-scale workpiece. Robot Comput Integr Manuf 2021;71:102153. https://doi.org/10.1016/j.rcim.2021.102153.
[32] Tsai PS, Wu TF, Chen JY, Tsai CL. Development of automated optical inspection and classifications systems. Sensors Mater 2022;34(10):3895–910. https://doi.org/10.18494/SAM4029.
[33] Jing X, Jiang H, Niu S, Zhang H, Gilbert Murengami B, Wu Z, et al. End-to-end stereo matching network with two-stage partition filtering for full-resolution depth estimation and precise localization of kiwifruit for robotic harvesting. Comput Electron Agric 2024;225:109333. https://doi.org/10.1016/j.compag.2024.109333.
[34] Jiang H, Gilbert Murengami B, Jiang L, Chen C, Johnson C, Auat Cheein F, et al. Automated segmentation of individual leafy potato stems after canopy consolidation using YOLOv8x with spatial and spectral features for UAV-based dense crop identification. Comput Electron Agric 2024;219:108795. https://doi.org/10.1016/j.compag.2024.108795.
[35] Xie S, Sun H. Tea-YOLOv8s: a tea bud detection model based on deep learning and computer vision. Sensors 2023;23:6576. https://doi.org/10.3390/s23146576.
[36] Mbouembe PLT, Liu G, Sikati J, Kim SC, Kim JH. An efficient tomato-detection method based on improved YOLOv4-tiny model in complex environment. Front Plant Sci 2023;14:1150958. https://doi.org/10.3389/fpls.2023.1150958.



Wulan Mao, Research Assistant, Institute of Agricultural Mechanization, Xinjiang Academy of Agricultural Sciences, Doctoral candidate (College of Mechanical and Electronic Engineering, Northwest A&F University, Electrification and Automation of Agriculture), Research on Forest Fruit Processing Equipment, and Email: maowulan@nwafu.edu.cn



Leilei He, Doctoral candidate (College of Mechanical and Electronic Engineering, Northwest A&F University, Electrification and Automation of Agriculture), Master Degree from the Northwest A&F University, Research on Intelligent Information Perception of Agriculture, and Email: hll2023@nwafu.edu.cn



Man Xia, Master candidate (College of Mechanical and Electronic Engineering, Northwest A&F University, Electrification and Automation of Agriculture), Bachelor Degree from the Anhui Agricultural University, Research on Intelligent Information Perception of Agriculture, and Email: manxia@nwafu.edu.cn



Hanhui Jiang, Master candidate (College of Mechanical and Electronic Engineering, Northwest A&F University, Electrification and Automation of Agriculture), Bachelor Degree from the Northwest A&F University, Research on Intelligent Information Perception of Agriculture, and Email: jianghanhui@nwafu.edu.cn



Rui Li, Laboratory technician, College of Mechanical and Electronic Engineering, Northwest A&F University, Doctoral Degree (College of Mechanical and Electronic Engineering, Northwest A&F University, Agricultural Mechanization Engineering), Research on Processing and Storage of Agricultural Products, and Email: ruili1216@nwafu.edu.cn



Ramesh Sahni, Scientist, Agricultural Mechanization Division, ICAR-Central Institute of Agricultural Engineering, Doctoral Degree, Research on Intelligent Information Perception of Agriculture, and Email: ramesh.sahni@icar.gov.in



Yaqoob Majeed, Assistant Professor, Department of Biological and Agricultural Engineering, Texas A&M University, Doctoral Degree, Research on Robot of Agriculture, and Email: yaqoob.majeed@ag.tamu.edu



Zhanjiang Zhu, Researcher, Institute of Agricultural Mechanization, Xinjiang Academy of Agricultural Sciences, Master's Degree (College of Mechanical and Electronic Engineering, Shihezi University, Agricultural Mechanization and Automation), Research on Forest Fruit Processing Equipment, and Email: zhuzhanjiang@xaas.ac.cn



Longsheng Fu, Professor, College of Mechanical and Electronic Engineering, Northwest A&F University, Key Laboratory of Agricultural Internet of Things, Ministry of Agriculture and Rural Affairs, Doctoral Degree (Hokkaido University, Science of environmental resources), Research on Agricultural Robotics, and Email: fulsh@nwafu.edu.cn